Improvements to multi-offset adaptive optics scanning laser ophthalmoscopy for *in vivo* imaging of individual retinal ganglion cell layer neurons in humans

Elena Gofas-Salas [1,*,†], Yuhua Rui [1,2,†], Pedro Mecê [1], Min Zhang [1], Valerie C. Snyder [1], Kari V. Vienola [1], Daniel Lee[3], José-Alain Sahel [1] and Ethan A. Rossi[1,3,4]

[1] *Department of Ophthalmology, University of Pittsburgh School of Medicine, Pittsburgh, PA, USA*
[2] *Eye center of Xiangya Hospital, Central South University; Hunan Key Laboratory of Ophthalmology; Changsha, Hunan, CHINA*
[3] *Department of Bioengineering, University of Pittsburgh Swanson School of Engineering, Pittsburgh, PA, USA*
[4] *McGowan Institute for Regenerative Medicine, University of Pittsburgh, Pittsburgh, Pennsylvania 15260, United States*
[*] *gofase@pitt.edu*

† Denotes that each of these authors contributed equally to this work.

Abstract:

Retinal ganglion cells (RGCs) are the primary output neurons of the retina. RGC dysfunction and death can cause irreversible vision loss in glaucoma and other ocular diseases. However, no methods exist to evaluate RGCs at the level of single cell in the living human eye in the clinic. Our aim is to implement a technique revealing the retinal ganglion cell layer neurons whose contrast, robustness and acquisition time would make it suitable for clinical diagnosis and monitoring of patients. While previously we were able to demonstrate high contrast imaging in monkeys, here we propose a new adaptive optics scanning laser ophthalmoscope configuration that allows us to achieve similar results on humans *in vivo*. In particular we used a new detection scheme that allowed us to switch from two light sources to one thereby enabling us to increase the light power, eliminate problems caused by chromatic aberration and improve the image registration process. Here we show that this optimized detection scheme and image processing pipeline improve the multi-offset technique for imaging of human RGC layer neurons.

1. Introduction

Retinal ganglion cells (RGCs) are neurons on the surface of the retina anterior to the photoreceptors. Their cell bodies receive visual information from the connections with other retinal neurons, including bipolar cells, and amacrine cells, and their long projecting axons form together to become the retinal nerve fiber bundles that carry the visual information and exit the eyeball to form the optic nerve [1]. RGCs are also involved in the neuro-degenerative process in many disorders, with their dysfunction and death resulting in irreversible vision loss [2]. However, current clinical diagnostic tools are still confined to detecting thinning of the whole ganglion cell layer or retinal nerve fiber layer (RNFL), and derive from there an estimate of the number of degenerated RGCs [3]. These techniques require a substantial proportion of RGCs to be lost (on the order of 10%) before statistically significant thinning of the RNFL can be detected [4], leading to higher probabilities of patients suffering irreversible vision loss before being diagnosed. The capability to routinely image human retinal neurons at the microscopic level in the living eye could open the door to a better understanding of neuro-degenerative diseases, such as glaucoma, Parkinson's disease and Alzheimer's disease [5–9]. This capability also has the potential to enable investigations into the pathogenesis and progress

of these diseases, improve early detection, as well as facilitate treatment evaluation and monitoring.

RGCs are challenging to image mainly because of their transparency compared to the photoreceptors, large vessels and the nerve fiber bundles. In addition, the layers of different cell types are in close proximity, requiring an imaging system with a high lateral and axial resolution using a modality able to enhance the contrast of these translucent cells. There are currently a few groups developing systems capable of optically revealing ganglions cells *in vivo* at a microscopic resolution. The two-photon microscope has been used on mouse and primate retina to produce structural contrast for nuclei and cellular features of RGCs *in vivo* through the detection of light emitted by endogenous fluorophores [10, 11]. However, the two-photon technique is significantly limited by the required high light levels for imaging, restricting its use to animals for now. Another technology targeting these cells, described by Liu *et al.* [12], is Adaptive Optics Optical Coherence Tomography (AO-OCT). This technique detects singly back-scattered light from transparent retinal tissue and is thought to exploit organelle motility inside ganglion cell somas to increase cell contrast. Although the authors were able to identify ganglion cell somas and estimate structural parameters such as soma density and diameter, their technique requires averaging images over a significant amount of time, making the translation to a clinical setting challenging. Finally, multi-offset imaging [11], in AO Scanning Laser Ophthalmoscopy (AO-SLO), uses multiply scattered light to achieve phase contrast in order to reveal the boundaries of these transparent cells. This technique belongs to a range of modalities based on non-confocal or off axis detection. Depending on the retinal structure of interest, different off-axis modalities were implemented on adaptive optics (AO) ophthalmoscopes, including AO Flood Illuminated Ophthalmoscope (AOFIO) [13, 14] or the AOSLO [15]. In the case of AOSLO, they mostly consist of shifting the confocal aperture from the center to block the single backscattered photons from highly reflective layers and detect the multiply scattered light that was forward scattered by retinal structures with low reflectivity. This simple configuration known as the offset aperture technique [16] reveals the wall structure of capillaries with great detail. On the other hand, the split detection configuration [17], which computes the normalized difference between the images obtained with the two sides of a detector divided by their sum , reveals the photoreceptor inner segments even when the outer segments are degenerated. Rossi *et al.* [11] combined the principle of these two techniques and developed multi-offset imaging by laterally displacing a pinhole around the optical axis and computing linear combinations between the images obtained at multiple positions. With this off-axis configuration we showed the first high resolution images of ganglion cells *in vivo* in the monkey and with lower SNR in the human retina. Achieving *in vivo* imaging of RGCs in humans was more challenging than on the monkey due to limitations of the imaging system. These limitations included the use of separate wavelengths for the confocal and multi-offset channels. Chromatic aberration between the different wavelengths made them offset both laterally and axially complicating focusing and introducing potential for error when using the confocal image to track the motion of the eye and applying that motion to the offset channels. Finally, the major limitation was simply the lower light levels that we used for imaging the humans compared to the monkeys, where monkey imaging was done using light levels higher than those that can be permitted in humans. This resulted in images with low SNR. Here, we addressed these limitations with an optimized AOSLO system able to perform robust *in vivo* imaging of RGCs in humans. We show the repeatability of this technique, which enables us to image different participants and eccentricities with a higher contrast and SNR than previously demonstrated in humans [11].

2. Methods

2.1. AOSLO system

Experiments were carried out on the Pittsburgh AOSLO described in detail elsewhere [18]. In summary, this AOSLO system has four sources for illumination and four detectors, three of which can be recorded simultaneously using custom electronics. These four detectors can be divided into three channels: A channel that records the near infrared autofluorescence signal at 832 nm wavelength, a confocal channel at 795 nm wavelength and a channel for the multi-offset detector. The selection of channels depends on the imaging protocol. In this study we use the detection path containing the confocal and multi-offset channels shown in Fig.1(a).

We illuminate the retina using a super-luminescent diode centered at 795 nm (FWHM=15nm) that is scanned in a raster fashion at 30 Hz to form a 1.5° ×1.5° field of view. The light scattered back from the retina is redirected towards the detection channels and then focused to a custom-made mask as shown in the schematic drawing in Fig. 1. This mask is composed of 11 elliptical gold mirrors, that act as circular reflective pinholes ranging from 1 to 10 Airy Disk Diameter (ADD) when the mask is placed at 45°angle with respect to the incoming beam. We set the beam at the reflective pinhole of 1 ADD (ϕ 27.7 μm) diameter. The central portion of the Gaussian beam is then directed to a Photomultiplier Tube (PMT) creating a confocal channel for the 795 nm beam. The remainder of the beam (outer portion) is relayed to another PMT, creating a second retinal conjugate focal plane for offset imaging. This second PMT was placed on motorized xyz-stages allowing precise control of the pinhole location in order to, first, automatically center the confocal pinhole and then, displaced in the xy plane to capture several offsets at different positions.

Compared to the previous multi-offset system developed by Rossi *et al.* [11], this instrument has been designed to facilitate use on human participants. A chin rest and a pair of forehead rests are used to stabilize the head. A pupil camera enables alignment of the position of the eye pupil in front of the beam. A fixation target is projected onto the retina for subject to follow, allowing imaging of different locations of the retina. The range of the visual angle accessible with the projector is limited to ±6°in all directions from the fovea.

A steering mirror has been implemented in the system to increase the range of the visual angle we can image. We use this mirror to displace the beam onto different regions of the retina, instead of asking the subject to constantly change fixation. The fixation target is placed at the center of the field of view for the first 6°eccentricities and at 5°in all directions to go above that range. Moreover, the combination of both a fixation target and steering control enabled us to increase the area of the retina accessible to imaging, with up to 30°in total maximum eccentricity that can be reached.

2.2. Image acquisition

2.2.1. Imaging protocol

We acquired several image sequences at each retinal location using different offset-aperture positions across the 2D retinal conjugate focal plane. We imaged at retinal eccentricities 5-14° (∼1.5–4 mm) temporal at the raphe and at 10-14° (∼3–4mm) nasal superior. We used a large pinhole (ϕ 200 μm, ∼ 7.5 ADD) at the multi-offset detector to increase the SNR of the images. A "radial" detection pattern was used, with apertures shifted to a fixed offset around the center. We tested several different radial patterns in a range of offsets from 6 to 12 ADD. We settled for an offset of 10 ADD and 8 aperture positions (see. Fig.1) which we empirically found to provide enough offset channel signal while still minimizing the directionally backscattered signal. Image sequences were acquired with an exposure time of 20s per aperture position for most experiments. However, we also evaluated the effect of exposure time with longer exposures up to 120 seconds.

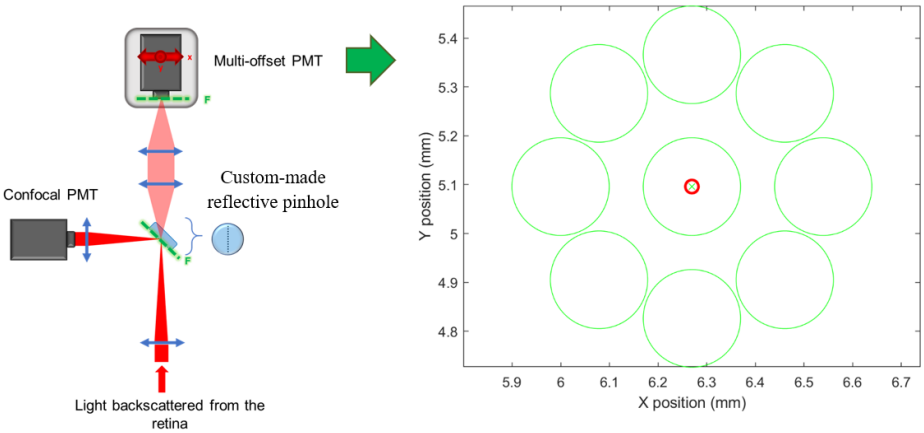

Fig. 1. Schematic drawing of the optical layout of the multi-offset detection path from the Pittsburgh AOSLO [18]: the light is physically separated with a custom made mask (this mask has 11 reflective pinholes and the beam is set on the one with a 1 Airy Disk Diameter (ADD) diameter) in order to image single-scattered light (confocal) and multiple scattered light (offset detection) simultaneously and with the same wavelength. The multi-offset photomultiplier (PMT) is placed on a motorized stage that is automatically set to follow in the xy plane the pattern indicated by the red arrow. The confocal pinhole in the center measures 27.7 μm or ~1 ADD (shown as a red circle) while the pinhole diameter of the off axis detection is 200 μm (~ 7.5 ADD). The offset apertures are at 10 ADD (shown as green circles) from the center and are separated by 45° between them.

2.2.2. Evaluating the effect of exposure duration for a single offset position

To improve image quality and to study the effect of exposure duration on the signal-to-noise ratio (SNR), we carried out a series of imaging session with longer exposure in 4 different offset positions. At each position, we acquired 6 sets of 20-second videos, 2 sets of 60-second videos, and a 120-second video.

2.3. Image processing

The sinusoidal artifact in the images was corrected using previously published methods [19] . Images were registered using the confocal 795 nm channel as reference with a strip-based image registration algorithm that is described in detail elsewhere [20]. We used Gullstrand simplified relaxed eye model to estimate the value of micron per degree depending on the axial length of the participant.

From each registered sequence obtained for each offset position we computed an average image. These averages are then linearly combined to enhance the phase contrast using the following relationship:

$$I_d = \frac{(I_i - I_j)}{(I_i + I_j)}, \tag{1}$$

where I_d is the obtained difference image and I_i and I_j are two averages generated from two different pinhole positions. The background contribution of the resulting difference image is

partially mitigated, but some low frequencies remain. To further mitigate the contribution of the background, a high pass filter with a normalized cut-off frequency of 0.2 is applied. Several difference images can then be averaged to generate enhanced contrast images of the cells. However, it should be noted that the polarity of the images should be matched prior to averaging or contrast can be reduced.

Finally, we enhanced the contrast of the cells by applying a Matlab built-in function Contrast-limited adaptive histogram equalization (CLAHE) with 9 by 9 number of tiles and 0.002 as the contrast enhancement limit.

2.4. Participants

For this study, 20 healthy participants were imaged (6 men and 12 women, ages ranging 20-64 yrs old). These participants are all free from eye conditions including congenital eye diseases, recent ocular infection, glaucoma, and recent eye surgery. They also had clear lens, deep and quiet anterior chambers, and a refractive error no more than -4D. Written informed consent was obtained from all participants following an explanation of experimental procedures and risks both verbally and in writing. All experiments were approved by the University of Pittsburgh Institutional Review Board and adhered to the tenets of the Declaration of Helsinki. All imaging light levels were under the ANSI laser safety [21] limits. To ensure these safety limitations we computed the Rochester Exposure Limit (REL), which is more restrictive than the ANSI safety limit, using the REL calculator [22]. All light levels were kept below the REL. Before each imaging session, we applied eye drops for pupil dilation (one drop of 1% Tropicamide; and one drop of 2.5% Phenylephrine Hydrochloride).

2.5. Data analysis

2.5.1. Computing the Power Density Spectrum

We computed the Power Density Spectrum (PSD) in order to display the spectral signature of the ganglion cell layer mosaic. Using Matlab, a 2D Fourier transform is applied to the image. Then, we computed the square of the modulus of the Fourier transform. A radial average is then generated and divided by the value of the zero frequency to display the normalized PSD over the spatial frequencies (in cycles per mm).

2.5.2. Computing the Spectral Signal-to-Noise Ratio

We computed the Spectral Signal-to-Noise Ratio (SSNR) of our average images to estimate the image quality. To obtain this metric we first generated two filtered images: the signal image, where we filtered the image around the spatial frequencies of interest (i.e close to the cell spacing) using the range [1,300] cycles per mm; and the noise image, where a high pass filter with a cutoff frequency of 500 cycles per mm was applied. Then, we computed the energy of those two images by extracting their variance. The SSNR value is generated by dividing the energy of the signal of interest by the energy of the noise. For each video we computed the SSNR of the images generated with various exposure times.

3. Results

Figure 2 shows an example of the resulting averages from one of our participants. In the center we have the confocal image (Fig.2 (e)) and surrounding it are eight offset images where the aperture was displaced by 10 ADD in a radial pattern. The schematic inset at the bottom right corner shows the position of the pinhole for each image. The fine cellular structure detected at each offset is modulated by the background and varies with the position of the aperture.

We also observe a strong signal of the background, similar to what we had observed previously in monkeys [11], that modulates the contrast of the cells. These low spatial frequencies appear to

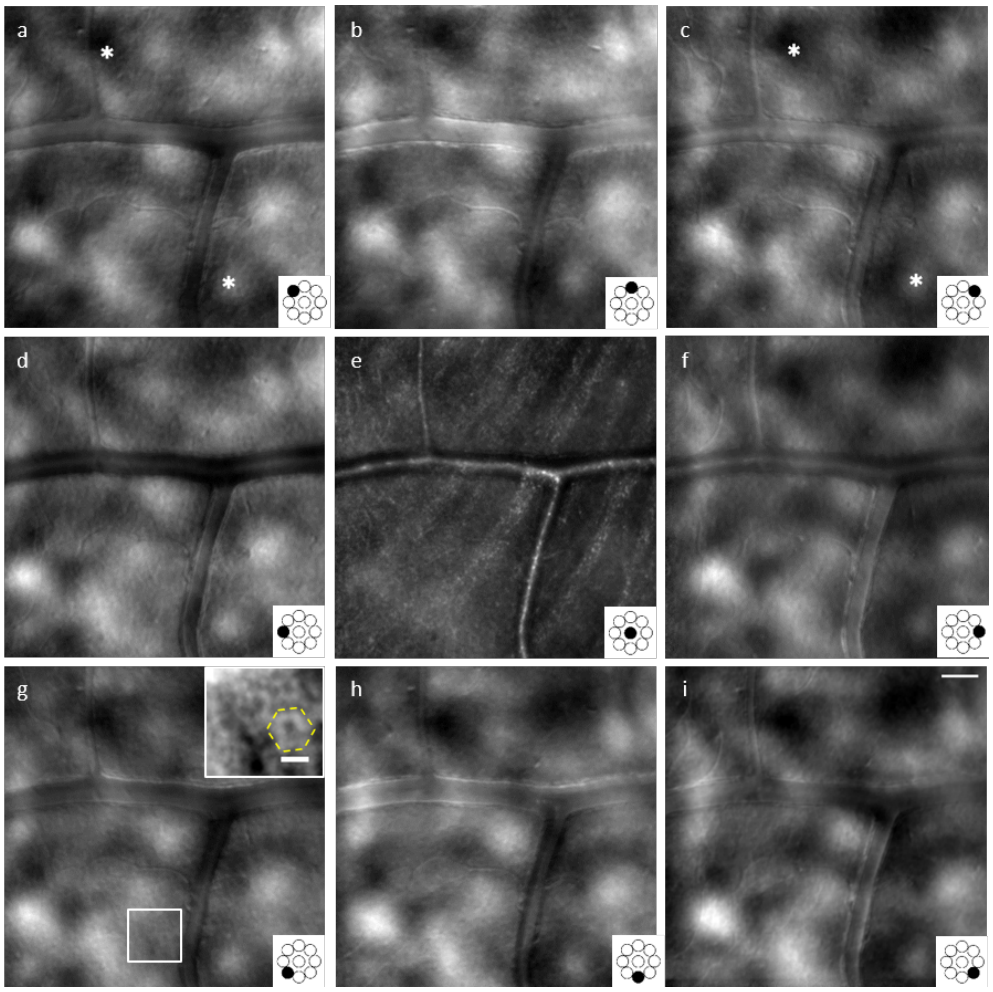

Fig. 2. Average images computed from the image sequences acquired at around 10° Temporal with the (e) confocal pinhole and the (a-d;f-i) surrounding offsets (Scale bar is 50 μm in (i)). A schematic drawing at the bottom left of every image indicates the position of the pinhole for each average. The asterisks denote the average center of darker and brighter areas that appear to be much closer to the nearest vessel in (a) and to have moved further away in (c). Enlarged region in (g) shows cell structure encircled by a yellow dashed line with a scale bar of 15 μm (in (g)).

carry a structural pattern but we observed that the background appears to shift depending on the position of the offset. For example, in Fig.2, the asterisks denote the average center of darker and brighter areas that appear to be much closer to the nearest vessel in a and to have moved further away in c.

In Fig.3 we compare the cellular structure in a single offset averaged image to difference images from two directions (oblique and vertical), and the average of these last two. Some cells, such as the one in Figs.3(e-h) indicated by a white arrowhead are revealed more clearly when computing the difference image. The difference image minimizes the background and increases the contrast of the cell as shown in Fig.3(j). This plot also shows a directionality of the signal as the contrast of the profile from the diagonal difference image (red curve) is enhanced with respect to the one from the vertical image (green curve).

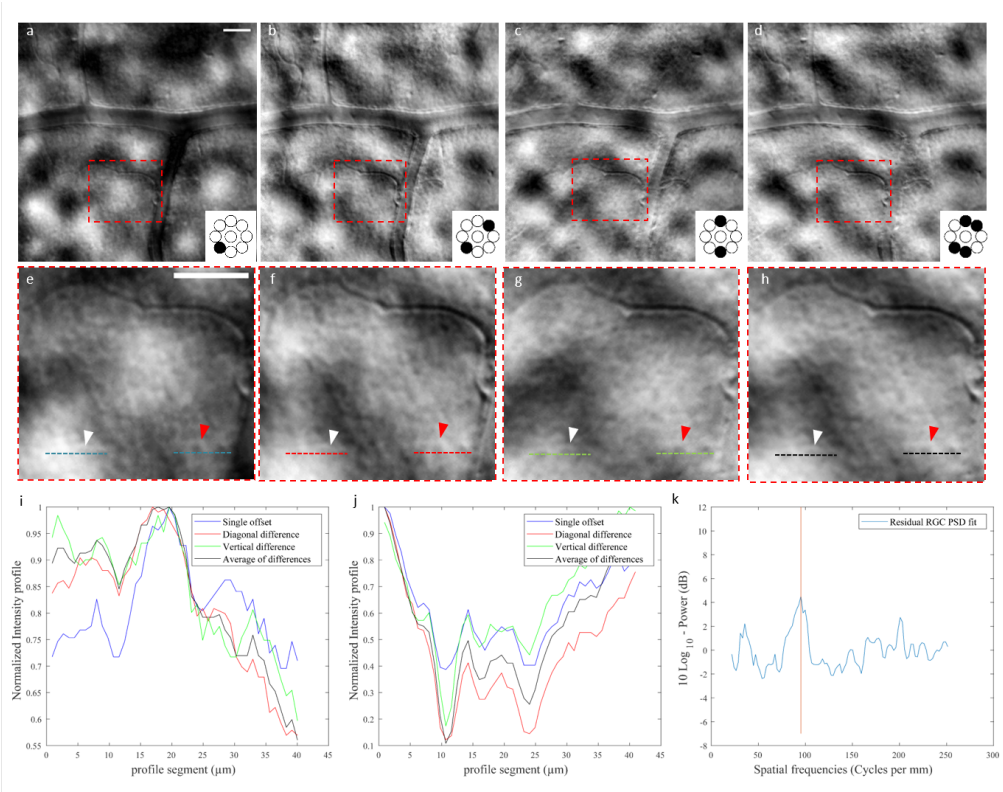

Fig. 3. (a) Average image obtained from a single offset. (b,c) Images computed from diagonal and vertical offsets respectively. (d) Average of (b,c) . (e-h) Enlarged region of (a-d) indicated with a red square. A red arrowhead indicates a cell whose contrast remains similar after computing the difference images and for which intensity profiles from the dotted segments are shown in (i). A white arrowhead shows a cells which is strongly modulated by the background and which is revealed in (b-d) when computing the differences. Its intensity profile for all images are shown in (j). (k) Logarithmic plot of the residual of the difference between the Power Spectrum Density of image (b) and its exponential fit. A peak is detected at a 100 cycles per mm (which corresponds to an average cell spacing of 12 μm). Scale bar is 50 µm.

It is interesting to notice that other cells, such as the one indicated in the same images by a red arrowhead is not substantially affected by the subtraction from the two pinholes and its contrast is already high enough to correctly identify the cell in the single offset (see cell profiles in Fig.3(i)).

Finally we show in Fig.3(k) the residual Power Spectrum Density (PSD) of image Fig.3(b) obtained from the difference between the actual PSD and its exponential fit. This computation enabled us to enhance the peak at the spatial frequency around the spacing of the cells revealed in the difference image. The elevation is centered at 92 cycles per mm, which corresponds to a cellular spacing of about 12.5 μm [23, 24].

We also tested the repeatability of our technique by generating two images of the cells in the same region, where the subject removed the head from the chin rest and rested between the image acquisitions. Figure 4 shows these two average images, which are linear combinations of the offsets . A red arrowhead indicates one of the many cells that can be identified in both images from the difference acquisitions, keeping the same contrast.

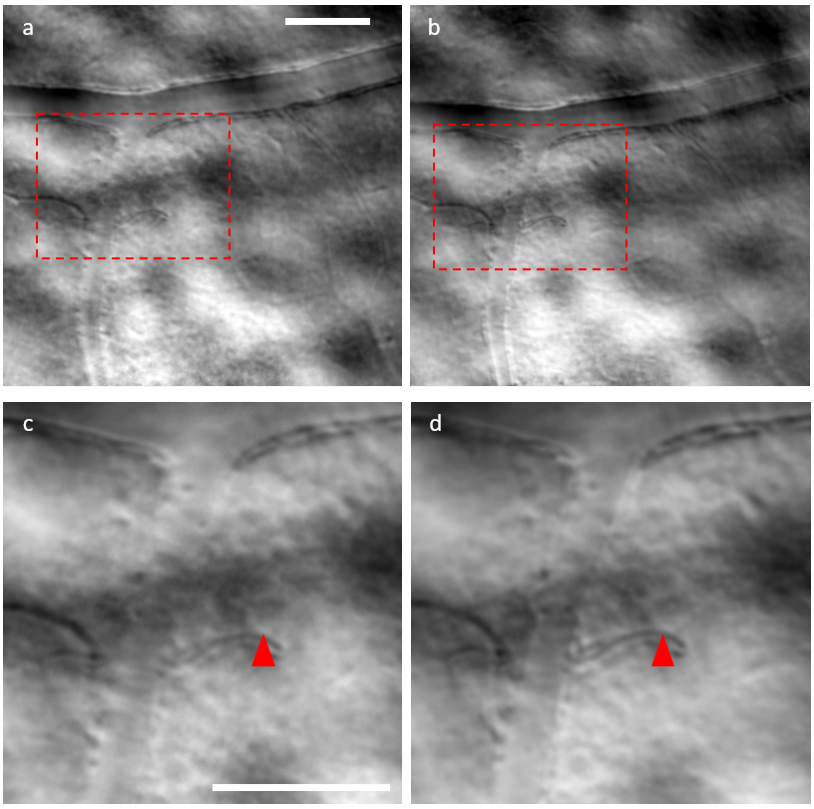

Fig. 4. (a,b) Average images combining several linear combination of pinholes from two different acquisitions.(c,d) Enlarged region from (a,b) indicating with a red arrowhead the same cell in both images.Scale bar are 50 μm.

In Fig.5 we show how cell contrast varies with exposure duration. We quantified this by using the SSNR as a metric. Figure 5 displays the SSNR as a function of the exposure time for one average image (left). We notice the increase of the metric's value with time, also corresponding to a gain in image quality of the enlarged region. The percentage of improvement between 1s and 10s was of around 80% while the increase significantly slowed down from an exposure time of 20s. We noticed that until 10s the contrast of the cells varied drastically from a very noisy and granulated image at 1s to a clear depiction of the cells at 10s. After about 20s of exposure time the improvement in subjective image quality was negligible, with cells displaying similar contrast at longer durations. Thus, it appears as though the optimal acquisition time is around 10-20 seconds per aperture position.

3.1. Summary of the technique

We acquired image sequences on several participants of different ages and across various eccentricities of the retina. In Fig.6 we show several examples of the cell mosaic obtained for various participants at three eccentricities. The contrast and diameters of these cells fall into the ganglion cell range of sizes found in the literature [12, 25]. This technique enabled us to image cells from the RGC layers on several participants with repeatable results.

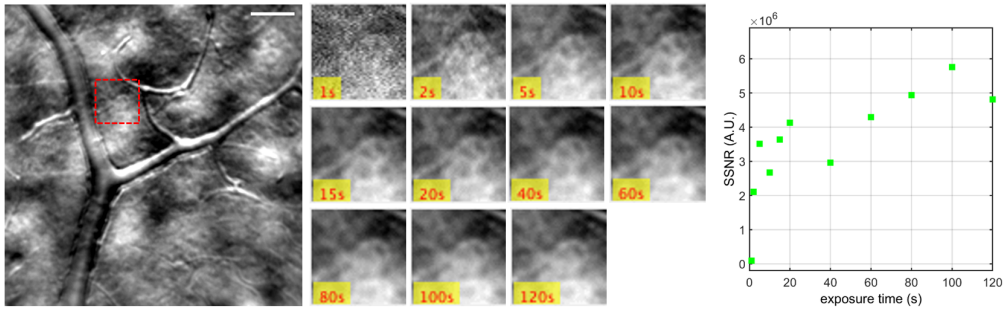

Fig. 5. (Left) Average image obtained from a single offset (histogram was stretched to increase the contrast). (Center) Enlarged region indicated by a dashed red square (47 μm x 47 μm) on the left averaged at different exposure times from the range [1s, 2s, 5s, 10s, 20s, 40s, 60s, 80s, 100s, 120s]. (Right) Plot of the Spectral Signal to Noise Ratio of the average image at the different exposure times. Scale bar is 50 μm.

4. Discussion

Our new multi-offset detection AOSLO optical setup has obviated some of the major limitations of our previous technique [11] and demonstrated robust, repeatable imaging of RGC layer neurons with relatively high-contrast in humans for the first time. This builds on our previous work and demonstrates that similar contrast levels to what we had shown previously only for anesthetized monkeys at high light levels can be obtained in awake behaving humans at safe light levels with relatively short duration exposures, on the order of 10 to 20 seconds per aperture position.

The principle behind this technique, previously described [26, 27], is to detect the phase signal of the photons after going through the cells by converting it into intensity at the detection plane. It is achieved by shifting the detection pinhole away from the center in different directions. The light going through the cells is deviated differently depending on the refractive indices and therefore photons from different regions of the cell do not reach the same offset aperture leading to differences between adjacent tissues with different refractive indexes in transparent cells [28].

The aim here was to overcome previous experimental limitations in order to improve the phase contrast signal of the ganglion cell layer in humans *in vivo*. By splitting the confocal and multi-offset detection channels with the custom-made reflective pinhole we were able to use the same imaging wavelength for both channels, in a similar way to nonconfocal split-detection [17]. This was a major improvement as it eliminated any possible blur induced from transverse chromatic aberration when using a different wavelength for confocal imaging and for tracking eye motion. We usually assume that there is a fixed Transverse Chromatic Aberration (TCA) between each imaging channel but changes in pupil position can change the TCA and this can be rendered as motion blur when assuming a fixed offset. This is not an issue when we use the same wavelength of light to track the eye as we do for the multi-offset imaging. Finally, unlike the previous experimental setup, here we have one imaging light source instead of two and with a longer wavelength. The use of a single near infrared imaging source permitted the use of higher light levels than for our previous multi-wavelength implementation of multi-offset imaging.

Figure 2 showed an example of the eight offset average images obtained after registration. The first thing to note about these images is the striking similarity in the overall contrast of both the cellular structures, as well as the vasculature and background, to what we had demonstrated previously in monkeys. We also note that there is a strong contribution from what we are describing as the background, which consisted of a pattern of bright and dark patches uniformly

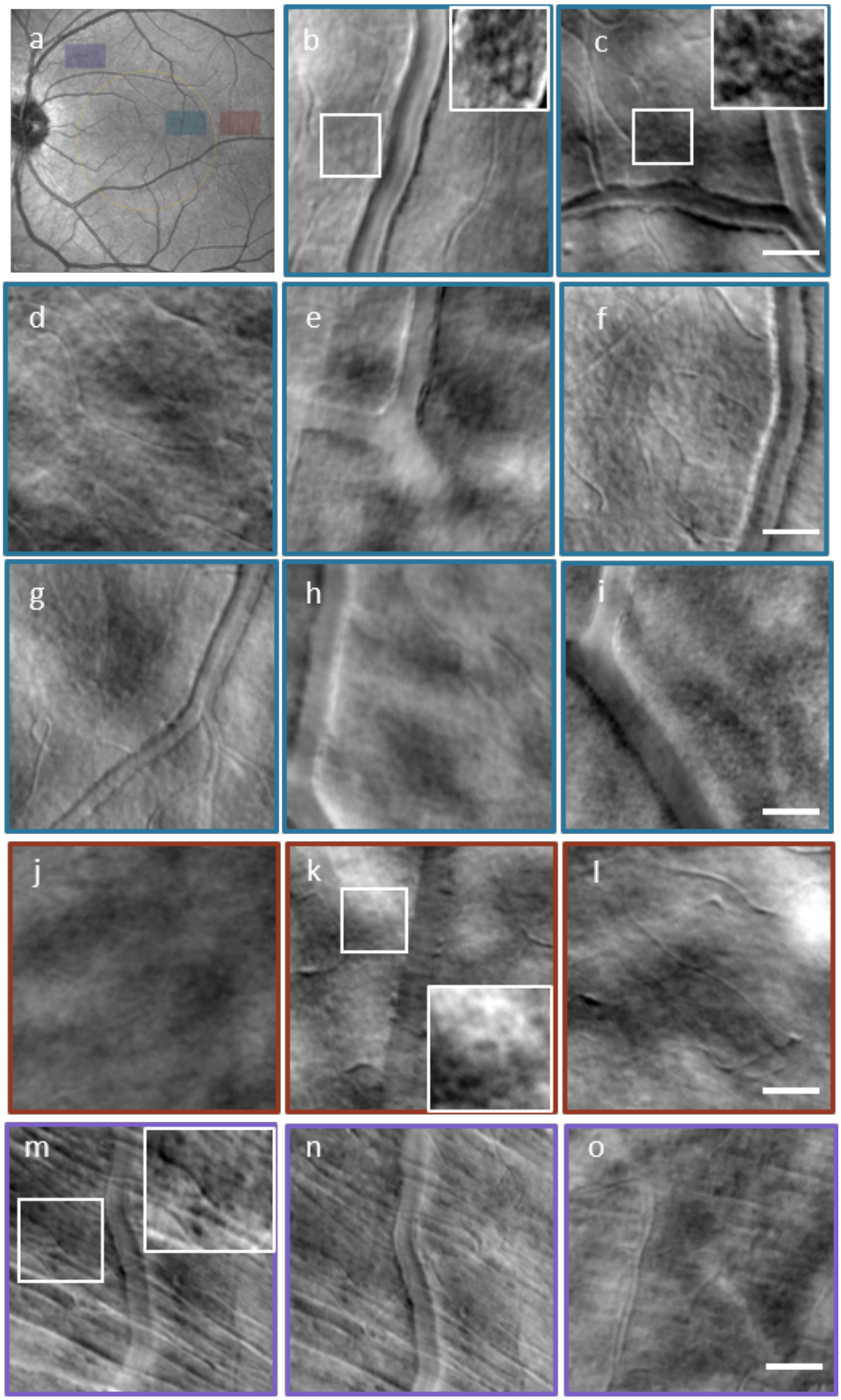

Fig. 6. Region of interest in average images obtained from several participants. (a) Typical SLO fundus showing the regions imaged on various participants: (b-i) Images obtained from around 3-5° Temporal (T) eccentricities, (j-l) from 8-12° T eccentricities, and (m-o) from 12° Nasal Superior eccentricities. Four enlarged regions in (b,c,k,m) show details of the cellular structure. Scale bars are 50 μm.

distributed at a low spatial frequency across all the images. In fact, the shape of the background remains the same in each of the eight offsets however, it is slightly shifted at each offset with respect to the vessel features in the images. The fact that the signal remains the same implies that it is likely due to scattering from a physiological structure. Based on the pattern and its diffuse out of focus appearance, we hypothesize that it may be from the choroid. Though this putative choroidal signal is an interesting feature that warrants further investigation, it was a drawback for our current imaging configuration where we were interested in creating phase contrast of RGC layer neurons.

In our current technique, which was inspired from phase contrast microscopy [29, 30] and from previous off-axis configuration in the ophthalmic community [16, 17, 31, 32], we generated what we call difference images by subtracting the images from the different offsets to cancel the background as well as absorption signals leaving only the phase signal. Moreover, the best phase contrast is theoretically generated by subtracting opposite pinholes, as with homogenous illumination they should lead to opposite phase values, and therefore double the signal when subtracted. However, as our background was not homogenous, we were unable to cancel it fully as can be seen in Fig.3 where the cell signal remained modulated by the low frequencies of the choroidal signal. This is likely due to the aforementioned apparent displacement of the low spatial frequency features of the background with change in aperture position. Future study should be directed towards improved methods to differentially enhance the contrast of these different structures.

Another effect impacting the image quality was the directionality of the phase contrast. The cellular structure displayed different contrast depending on the position of the aperture. In Fig.3 the difference image obtained with the apertures in the vertical direction leads to a lower contrast of the cell (see green curve of cell profile in Fig.3 (j)), indicated by white arrowhead, than with the apertures in the diagonal direction (see red curve). This difference is due to the variation of the amount of photons deviated in one direction with respect to another. We noticed some cells displayed similar contrast for different subtraction directions. Fig.3 (i) shows the profiles of a cell from images obtained with various pinholes and subtraction directions whose contrast remains very similar. These two effects highlighted the importance of smartly combining the images obtained from each aperture to avoid weakening the cell signal.

A well-known method to characterize the cone photoreceptor mosaic is to compute the Fourier Transform (FT) and evaluate Yellot's ring [23, 33]. Though we do not anticipate the RGCs to be as regularly arranged as the cones, we chose this method to serve as a signature of the size of the cellular structures visible in the images. We evaluated the energy distribution of our images, particularly around the spatial frequencies close to the range we expected for the spacing of retinal ganglion cells. The increase in energy shown in Fig. 3 is significantly wider and lower than the peaks typically observed on the PSD of photoreceptors images. This is due to the fact that the contrast of photoreceptor images is higher and their mosaic is more regularly spaced than these cells from the RGC layer. This leads to higher amount of energy concentrated in a particular spatial frequency. On the other hand, the RGC soma diameter can range from 6 μm to 25 μm [12, 25, 34, 35] leading to the distribution of the energy in a larger range of spatial frequencies, and therefore to a flatter elevation.

We also investigated whether image quality could be improved by increasing the acquisition time at each offset position. The image quality metric SSNR plotted in Fig.5 showed a rapid increase in the contrast of the cells, reaching a stable SSNR value at around 10s, which also corresponds to the average image where the cluster of cells shown in Fig.5 became less noisy and where the cells were resolved. The short exposure time necessary to obtain a good image quality of the cells combined with an automatizing of the steering mirror could enable us to

achieve in just a few minutes a reconstructed large field of view of the RGC layer. In addition, participants don't need to fixate for a long period of time, making this technique particularly suited for the clinic. This short timescale could also enable us to monitor the cellular dynamics under a minute of these cells. Although we reach a lower cell contrast than what is obtained with AO-OCT, we do not require averaging several data sequence acquisitions, which might make this technique more suitable to monitor patient diseases. We also verified that the effect of the fatigue of the participant did not show any significant difference between outputs from one single long acquisition or concatenated ones. Morevover, two averages generated from two of these different acquisitions showing the same cells in Fig.4 outline the robustness and repeatability of the technique.

We imaged 20 participants, from whom some were elderly participants or had some difficulties to fixate for long periods of time. The improved registration custom algorithm described by [20] helped mitigate the increased amount of distortion artifacts generated in these cases of important eye motion. Figure 6 shows a selection of images from all the participants on three different regions obtained with the multi-offset technique. We notice how, similar to offset and split-detection configurations, low contrast features stand out. In images like Fig.6(c,e,g), the vessel wall contrast is enhanced so that details of the different layers can be resolved and therefore quantified. In others like Fig.6(m-o) obtained on the nasal region, which has thicker nerve fiber layer, one can distinguish single fiber bundles.

Moreover, we identified what looks like cell somas attached to some of these bundles (see enlarged region in Fig.6(m)). These putative somas could be quantified on healthy and patients suffering from nerve fiber degeneration in order to evaluate the amount of cell loss that could be detected using this technique.

The contrast of these fibers, as well as other features like the vessel wall or capillaries, is dependent on the orientation of the offset detector position with respect to the orientation of the retinal structures. Since the orientation of these retinal features vary with eccentricity, it is necessary to acquire in multiple offset positions to ensure their detection at high contrast at all eccentricities.

We also noticed the differences in the appearance of the cells at the different retinal eccentricities. In Fig.6(b) we see smaller circular adjacent cells while in a similar eccentricity of 5T in Fig.6(c) the cells display a dark center surrounded by a brighter ring. This latter contrast is also observed in 6(k) at a further eccentricity of 10T in another cluster of cells. Our hypothesis is that depending on the polarity of the image the center of the cell will appear bright or dark, and one can simply invert the image to convert one into the other. However it is interesting to notice that sometimes different polarities are observed in the same image, which is most likely due to non uniformity in the scattered light introduced by adjacent retinal features, such as vessels. In nasal eccentricities where the thickness of the retina is greater, the cells are more difficult to image. In Fig.6(m) we see some cells interdigitated between the fibers. This is consistent with images of RGCs in histology [34, 35] and in our prior work [11].

Although we have significantly improved the cellular contrast of the RGCs with presented technical optimization, we are still facing a few limitations. Despite the fact that RGCs were visible in many areas of the field of view for several participants, we still have regions where we do not seem to reach a contrast high enough to clearly identify the cells. We are currently working to further enhance the contrast of these missing regions by developing improved image processing techniques.

We are also working to implement machine learning algorithms that could detect weak signals and segment the cells, including even those withe low contrast. In addition , it was demonstrated on mice that the contrast of cells in off axis technique can be improved by conjugating the detector plane with a deeper highly backscattering layer of the retina (which was the retinal

pigment epithelium (RPE)) instead of the sample plane (here the RGC layer) [28]. They showed that contrast for imaging mouse horizontal cells was improved when displacing the detector to a deeper plane conjugated to the RPE and hypothesized that a smaller but still substantial improvement might be achieved with a similar approach in humans. If this prediction from mice holds for humans, then it is possible that displacement of the detector to a deeper retinal plane may result in improved cell contrast.

Finally we are moving from our sequential acquisition to a simultaneous acquisition by implementing our current detection pattern with a fiber bundle. This new configuration will allow us to decrease the acquisition time substantially, as all offsets can be acquired simultaneously. This will permit multi-offset images to be obtained in just 10-20 seconds and therefore could be used to monitor cellular changes over short periods of time (minutes). This will facilitate the imaging of larger areas and makes the prospect of clinical imaging much more feasible.

5. Conclusion

We optimized our previous optical system to mitigate the impact of technical limitations such as chromatic aberrations or eye motion, which prevented us from reaching high contrast images of RGCs in humans such as the ones obtained in the monkey. We demonstrated the capabilities of the multi-offset imaging technique to achieve repeatable high contrast images of these retinal cells at different eccentricities and participants. The estimated exposure time, as short as 10s, necessary to reach this contrast makes this technique suitable for the clinic where the study of the RGCs on degenerated retinas could be used to study retinal pathologies such as glaucoma. We predict that with some additional improvements, such as simultaneous detection, multi-offset imaging may one day provide a powerful tool to evaluate the earliest abnormalities and temporal sequence of changes that precede and accompany RGC death in glaucoma and other neurodegenerative diseases.

Funding

This research was supported by a National Glaucoma Research Award from the BrightFocus Foundation (G2017082) to Ethan A. Rossi. It was also partially supported by a grant from Foundation Fighting Blindness (PPA-081900772-INSERM) and by departmental startup funds from the University of Pittsburgh to Ethan A. Rossi. This work was also supported by NIH CORE Grant P20 EY08098 to the University of Pittsburgh Department of Ophthalmology, the Eye and Ear Foundation of Pittsburgh, the NVIDIA GPU Grant Program, and from an unrestricted grant from Research to Prevent Blindness, New York, N.Y. USA.

Acknowledgments

The authors would like to thank Austin Roorda for sharing his AOSLO software with us and Pavan Tiruveedhula for electronics fabrication, software, and technical assistance.

Disclosures

Ethan A. Rossi has patents on some aspects of the technologies used to carry out these experiments (US10,772,496; US10,123,697; & US10,092,181).

References

1. H. Kolb, "Simple anatomy of the retina by helga kolb," Webvision: The Organ. Retin. Vis. Syst. (2011).
2. D. García-Ayuso, J. Di Pierdomenico, M. Vidal-Sanz, and M. P. Villegas-Pérez, "Retinal ganglion cell death as a late remodeling effect of photoreceptor degeneration," Int. journal molecular sciences **20**, 4649 (2019).

3. K. Hirooka, S. Izumibata, K. Ukegawa, E. Nitta, and A. Tsujikawa, "Estimating the rate of retinal ganglion cell loss to detect glaucoma progression: An observational cohort study," Medicine **95** (2016).
4. T. Rolle, L. Dallorto, and B. Bonetti, "Retinal and Macular Ganglion Cell Count Estimated With Optical Coherence Tomography RTVUE-100 as a Candidate Biomarker for Glaucoma," Investig. Ophthalmol. & Vis. Sci. **57**, 5772–5779 (2016).
5. H. A. Quigley, G. R. Dunkelberger, and W. R. Green, "Retinal ganglion cell atrophy correlated with automated perimetry in human eyes with glaucoma," Am. journal ophthalmology **107**, 453–464 (1989).
6. P. K. Iseri, Ö. Altinas, T. Tokay, and N. Yüksel, "Relationship between cognitive impairment and retinal morphological and visual functional abnormalities in alzheimer disease," J. neuro-ophthalmology **26**, 18–24 (2006).
7. C. La Morgia, F. N. Ross-Cisneros, A. A. Sadun, and V. Carelli, "Retinal ganglion cells and circadian rhythms in alzheimer's disease, parkinson's disease, and beyond," Front. neurology **8**, 162 (2017).
8. R. Inzelberg, J. A. Ramirez, P. Nisipeanu, and A. Ophir, "Retinal nerve fiber layer thinning in parkinson disease," Vis. research **44**, 2793–2797 (2004).
9. I. Ortuño-Lizarán, G. Esquiva, T. G. Beach, G. E. Serrano, C. H. Adler, P. Lax, and N. Cuenca, "Degeneration of human photosensitive retinal ganglion cells may explain sleep and circadian rhythms disorders in parkinson's disease," Acta neuropathologica communications **6**, 1–10 (2018).
10. R. Sharma, D. R. Williams, G. Palczewska, K. Palczewski, and J. J. Hunter, "Two-photon autofluorescence imaging reveals cellular structures throughout the retina of the living primate eye," Investig. ophthalmology & visual science **57**, 632–646 (2016).
11. E. A. Rossi, C. E. Granger, R. Sharma, Q. Yang, K. Saito, C. Schwarz, S. Walters, K. Nozato, J. Zhang, T. Kawakami *et al.*, "Imaging individual neurons in the retinal ganglion cell layer of the living eye," Proc. Natl. Acad. Sci. **114**, 586–591 (2017).
12. Z. Liu, K. Kurokawa, F. Zhang, J. J. Lee, and D. T. Miller, "Imaging and quantifying ganglion cells and other transparent neurons in the living human retina," Proc. Natl. Acad. Sci. **114**, 12803–12808 (2017).
13. E. Gofas-Salas, P. Mecê, L. Mugnier, A. M. Bonnefois, C. Petit, K. Grieve, J. Sahel, M. Paques, and S. Meimon, "Near infrared adaptive optics flood illumination retinal angiography," Biomed. optics express **10**, 2730–2743 (2019).
14. P. Bedggood and A. Metha, "Adaptive optics imaging of the retinal microvasculature," Clin. Exp. Optom. **103**, 112–122 (2020).
15. S. A. Burns, A. E. Elsner, K. A. Sapoznik, R. L. Warner, and T. J. Gast, "Adaptive optics imaging of the human retina," Prog. Retin. Eye Res. **68**, 1 – 30 (2019).
16. T. Y. Chui, D. A. VanNasdale, and S. A. Burns, "The use of forward scatter to improve retinal vascular imaging with an adaptive optics scanning laser ophthalmoscope," Biomed. optics express **3**, 2537–2549 (2012).
17. D. Scoles, Y. N. Sulai, C. S. Langlo, G. A. Fishman, C. A. Curcio, J. Carroll, and A. Dubra, "In vivo imaging of human cone photoreceptor inner segments," Investig. ophthalmology & visual science **55**, 4244–4251 (2014).
18. K. V. Vienola, M. Zhang, V. C. Snyder, J.-A. Sahel, K. K. Dansingani, and E. A. Rossi, "Microstructure of the retinal pigment epithelium near-infrared autofluorescence in healthy young eyes and in patients with amd," Sci. Reports **10**, 1–10 (2020).
19. Q. Yang, L. Yin, K. Nozato, J. Zhang, K. Saito, W. H. Merigan, D. R. Williams, and E. A. Rossi, "Calibration-free sinusoidal rectification and uniform retinal irradiance in scanning light ophthalmoscopy," Opt. letters **40**, 85–88 (2015).
20. M. Zhang, E. Gofas-Salas, B. T. Leonard, Y. Rui, V. Snyder, H. Reecher, P. Mecê, and E. A. Rossi, "Improvements to strip-based digital image registration for robust eye-tracking and to minimize distortions in images from scanned ophthalmic imaging systems," bioRxiv (2020).
21. L. I. of America, "American national standard for safe use of lasers,ansi z136.1," (2014).
22. E. A. Rossi and J. J. Hunter, "Rochester exposure limit calculator [computer software]," http://aria.cvs.rochester.edu/software/RELcalculator.html/ (2013). [Online; accessed May-2019].
23. R. F. Cooper, C. S. Langlo, A. Dubra, and J. Carroll, "Automatic detection of modal spacing (yellott's ring) in adaptive optics scanning light ophthalmoscope images," Ophthalmic Physiol. Opt. **33**, 540–549 (2013).
24. K. Y. Li, P. Tiruveedhula, and A. Roorda, "Intersubject variability of foveal cone photoreceptor density in relation to eye length," Investig. ophthalmology & visual science **51**, 6858–6867 (2010).
25. C. A. Curcio and K. A. Allen, "Topography of ganglion cells in human retina," J. comparative Neurol. **300**, 5–25 (1990).
26. Y. N. Sulai, D. Scoles, Z. Harvey, and A. Dubra, "Visualization of retinal vascular structure and perfusion with a nonconfocal adaptive optics scanning light ophthalmoscope," JOSA A **31**, 569–579 (2014).
27. D. Cunefare, R. F. Cooper, B. Higgins, D. F. Katz, A. Dubra, J. Carroll, and S. Farsiu, "Automatic detection of cone photoreceptors in split detector adaptive optics scanning light ophthalmoscope images," Biomed. optics express **7**, 2036–2050 (2016).
28. A. Guevara-Torres, D. Williams, and J. Schallek, "Origin of cell contrast in offset aperture adaptive optics ophthalmoscopy," Opt. Lett. **45**, 840–843 (2020).
29. D. Hamilton, C. Sheppard, and T. Wilson, "Improved imaging of phase gradients in scanning optical microscopy," J. microscopy **135**, 275–286 (1984).
30. T. N. Ford, K. K. Chu, and J. Mertz, "Phase-gradient microscopy in thick tissue with oblique back-illumination," Nat. Methods **9**, 1195–1197 (2012).

31. R. H. Webb, G. W. Hughes, and F. C. Delori, "Confocal scanning laser ophthalmoscope," Appl. optics **26**, 1492–1499 (1987).
32. A. E. Elsner, S. A. Burns, J. J. Weiter, and F. C. Delori, "Infrared imaging of sub-retinal structures in the human ocular fundus," Vis. research **36**, 191–205 (1996).
33. J. I. Yellott, "Spectral analysis of spatial sampling by photoreceptors: topological disorder prevents aliasing." Vis. research **22**, 1205–1210 (1982).
34. R. Rodieck, K. Binmoeller, and J. Dineen, "Parasol and midget ganglion cells of the human retina," J. Comp. Neurol. **233**, 115–132 (1985).
35. A. Harman, B. Abrahams, S. Moore, and R. Hoskins, "Neuronal density in the human retinal ganglion cell layer from 16–77 years," The Anat. Rec. An Off. Publ. Am. Assoc. Anat. **260**, 124–131 (2000).